Research Square

Preprints are preliminary reports that have not undergone peer review.
They should not be considered conclusive, used to inform clinical practice,
or referenced by the media as validated information.

Evaluation of Thermal Cycles and Microstructure in an ER2209 Stainless Steel Preform Fabricated by the WAAM-GMA Process

Luis Luigiouv Kirvdoff Vargas del Aguila

luisluigiouv@outlook.es

FURG: Universidade Federal do Rio Grande https://orcid.org/0009-0009-6434-6872

Kleber Eduardo Bianchi

FURG: Universidade Federal do Rio Grande

Daniel Souza

Universidade Federal de Goiás

Sabrina Espinosa Cabrera

FURG: Universidade Federal do Rio Grande

Thais Andrezza dos Passos

FURG: Universidade Federal do Rio Grande

Research Article

Keywords: Wire Arc Additive Manufacturing, Duplex stainless steels, Thermal cycles, Thermal camera, Computer Vision

Posted Date: August 5th, 2026

DOI: https://doi.org/10.21203/rs.3.rs-10580019/v1

License: This work is licensed under a Creative Commons Attribution 4.0 International License.
Read Full License

Additional Declarations: The authors declare no competing interests.

Evaluation of Thermal Cycles and Microstructure in an ER2209 Stainless Steel Preform Fabricated by the WAAM-GMA Process

Luis Luigiouv Kirvdoff Vargas del Aguila[1*], Kleber Eduardo Bianchi[1†], Daniel Souza[2†], Sabrina Espinosa Cabrera[1†] and Thais Andrezza dos Passos[1†]

[1*]School of Engineering, Federal University of Rio Grande, Av. Itália s/n km 8, bairro Carreiros, Rio Grande, 96203-900, Rio Grande do Sul, Brazil.
[2]School of Mechanical, Electrical and Computer Engineering, Federal University of Goiás, Avenida Esperança s/n, Goiânia, 74690-900, Goiás, Brazil.

*Corresponding author(s). E-mail(s): luisluigiouv@outlook.es;
Contributing authors: bianchi.kleber@gmail.com; daniel.souza@ufg.br;
sabrinaespinosa19@outlook.com; thais.andrezza.passos@gmail.com
†These authors contributed equally to this work.

Abstract: Wire Arc Additive Manufacturing (WAAM) of duplex stainless steels aims to produce parts and structures with complex and optimized geometries that can operate in chemically aggressive environments. However, when using this material in WAAM, the application of multiple thermal cycles alters the ferrite-to-austenite ratio, which ideally should be 1:1. In this study, an ER2209 duplex stainless steel wire was employed for the WAAM-GMA fabrication of a preform consisting of 50 continuously deposited layers. The complete thermal cycle in the central region of the preform was monitored using a thermal camera, for which specialized software was developed. Temperature data were collected at three heights: *i)* near the base plate, *ii)* at the mid-height of the wall, and *iii)* within the last deposited layers. These measurements were compared with a pseudo-binary Fe-Cr-Ni diagram with 70% iron content, as well as a time-temperature diagram of precipitate formation. These same regions were subjected to hardness test and phase quantification analysis, and the data set was analyzed and correlated with the thermal cycles. The results indicated that using WAAM-GMA without proper control of heat input led to austenite content exceeding 70%, which is unacceptable for duplex stainless steel. Additionally, there were signs of potential precipitation of harmful phases, and undesirable geometric variations were observed in the fabricated wall.

Keywords: Wire Arc Additive Manufacturing; Duplex stainless steels; Thermal cycles; Thermal camera; Computer Vision.

1 Introduction

The transition from mass production to customized manufacturing has been a goal since the beginning of the 20th century [1]. This transition has become possible through the consolidation of CAx (Computer Aided Design/Analysis/Manufacturing) and DFx (Design for Manufacturing/Assembling/Environment), as well as the collection and processing of large amounts of data by supercomputers and ERP (Enterprise Resource Planning) softwares. Finally, tools such as the Internet of Things and Artificial Intelligence have contributed significantly to accelerating the process [2–4].

Additive manufacturing (AM) allows the production of customized parts with complex geometries, which are difficult to manufacture by other means [5,6]. In the case of metallic materials, electric arc fusion processes offer raw material savings and high deposition rates, which has generated interest in sectors that produce complex and large-scale parts or structures, such as the aerospace, petrochemical, railway, automotive, civil construction, and architectural industries [6,7].

In addition to WAAM, additive manufacturing technics based on metal fusion also encompasses Selective Laser Melting (SLM), Electron Beam Melting (EBM), and Laser Metal Deposition (LMD) [8–11]. However, WAAM stands out due to its high material deposition rate, which typically ranges from 1 to 4 kg/h [7,12,13], and can exceed this range. For instance, Han et al. [14] employed an auxiliary wire to achieve rates up to 4.7 kg/h in

the fabrication of 10-layer H08Mn2Si walls.

Controlling the microstructure in WAAM is complex due to the influence of welding parameters and heat accumulation along the layer's deposition [6,15]. Thermal management techniques have been developed to control heat input, aiming to avoid undesirable metallurgical transformations and mitigate the level of residual stress. In these techniques, the temperature for deposition of a new layer is one of the main goals, which can be achieved, for example, with Quasi-Immersion Active Cooling [6,16].

Among the various materials of interest, both for WAAM and for the field of structures in general, stainless steel stand out, and especially duplex alloys. Developed since the 1980s, these alloys have been progressively employed in a wide variety of applications, as they exhibit good mechanical properties with high resistance to chloride stress-corrosion cracking [17]. One key industrial sector interested in this type of material is the manufacturing of bridges and other civil structures [18–20].

The commercial name duplex comes from its metallurgical structure, composed of austenitic and ferritic phases in approximately equal proportions [21]. In general, duplex alloys have a higher chromium content (18-30%) compared to austenitic stainless steels, but a lower proportion of nickel (1-9.5%). In addition, molybdenum (0.1-5%) and nitrogen (0.05-0.50%) are important elements in the composition [17].

The various duplex stainless steels are characterized based on a Fe-Cr-Ni-N system, whose contents are adjusted to obtain an approximate proportion of 50% austenite and 50% ferrite [22]. Fe-Cr-Ni-N diagrams are commonly used to determine the microstructure of stainless steels and are referenced by the ratio of chromium and nickel equivalent contents [Cr_{eq}/Ni_{eq}], which, in turn, are obtained using equations 1 and 2 [23].

$$Cr_{eq}=Cr+Mo+0,7Nb \quad (1)$$

$$Ni_{eq}=Ni+35C+20N+0,25Cu \quad (2)$$

From a manufacturing standpoint, the production of duplex alloys is relatively complex, as the material presents low ductility in the hot rolling temperatures and is also prone to the formation of brittle phases. The π phase, α′ phase, χ phase, and M_7C_2 carbide are among the various precipitates that can form at temperatures ranging from approximately 300 °C to 1000 °C, and they are responsible for impairing the mechanical properties and corrosion resistance of duplex stainless steels [22]. These conditions render hot forming of thin sheets and profiles impractical, which is resolved by using multiple stages of cold rolling, interspersed with annealing treatments.

Finally, regarding the use of duplex alloys in the production of welded parts and structures, specific techniques must be employed to avoid excessive imbalance in the resulting phase ratio [21,24].

Given this scenario, the present work reports experiments in which the WAAM-GMA technique was employed, in conjunction with a computer vision system for temperature monitoring, to fabricate a preform (straight vertical wall), composed of 50 layers, using an addition metal corresponding to the ER2209 duplex alloy. The captured thermal cycles were compared with the microstructure observed in samples taken from the preform, on which the phases were quantified. These analyses were complemented by hardness tests.

The analysis of the results considered the work of Hejripour et al. [25], in which the authors fabricated ER2209 alloy preforms using a semi-automatic GMAW process, monitoring the temperature using thermocouples and comparing the results with those obtained by numerical simulation. The deposition strategy used by the authors was a continuous zigzag pattern, without stops; however, the displacement speed was incrementally reduced from the third layer onwards, to mitigate heat accumulation. Even so, an increase in temperature peaks was observed throughout the deposition, with a consequent increase in the proportion of austenite.

This increase in the proportion of austenite with the advancement of the deposition process was also observed by Karunanithi et al [26]. Seeking to evaluate the mechanical properties and electrochemical behavior of the resulting material, the authors produced a wall with 100 layers, adopting an electrode compatible with the ER 2209 alloy, as well as an interpass temperature of approximately 150 °C.

2 Materials and Methods

2.1 Materials and main equipments

The filler metal consisted of a 1 mm diameter wire of ER2209 alloy, while a 19 mm thick ASTM A36 structural steel plate with side dimensions of 250x250 mm was used as the substrate. The compositions of these materials are shown in Table 1.

Table 1. Chemical composition of the deposition material and the substrate (wt%) [26,27].

Material	Al	Cu	Cr	Mn	Mo	Nb	Ni	Si	C	N	P	S	Fe
ER2209	0,01	0,05	22,9	1,54	3,1	-	9	0,53	0,025	0,16	0,02	0,005	Bal.
ASTM A36	-	0,2	-	1,03	-	-	-	0,4	0,26	-	0,04	0,05	Bal.

The relatively large dimensions of the baseplate were established to mitigate deformations caused by heat input, which can affect the deposition process [28].

The computer vision system was developed to operate effectively in an industrial environment, prioritizing low cost and an intuitive user interface. The thermal camera used, an InfiRay P2 Pro model, has a resolution of 256x192 pixels, a pixel size of 12 µm, and a frame rate of 25 Hz. The temperature range captured extends from -20 °C to 600 °C. Since the WAAM process generates high temperatures, exceeding the camera's operating range, a 10 % transmissivity filter with a diameter of 25 mm was used. This filter allowed the camera to capture temperatures up to 1500 °C; however, this required calibrating the temperature reading based on data provided by type K thermocouples.

The WAAM-GMA preform fabrication process was carried out by a Yaskawa MOTOMAN HP20D robot with 6 axes of movement, in conjunction with a DigiPLUS A7 multiprocess welding power source. Current and voltage were monitored throughout the deposition process by a data acquisition system. The shielding gas consisted of a mixture of carbon dioxide (8 %) and argon (92 %). The authors were aware that such a mixture would not be recommended for the wire used, due to its reactivity with chromium, which would cause a decrease in the oxidation and corrosion resistance of the deposited material [29]. As the present work focused on the heat regimes imposed on the material and their correlation with the microstructure, it was understood that the use of a lower-cost shielding gas would not compromise the results.

An Olympus GX51F optical microscope, serial number 0F68306, was used in conjunction with a Hayear 5130 camera to capture images of the metallographic samples. Finally, the hardness tests were performed with a Zwick ZHU187.5/ZHV30 universal.

2.2 Methodology

The preform was fabricated in the center of the base plate, to provide uniform heat dissipation. The layer height, and consequently the robot vertical increment per layer, was determined through preliminary tests using a 20-layer preform.

A zigzag deposition strategy was employed continuously, without stopping. This strategy is commonly used in WAAM due to its productivity benefits and its ability to prevent weld discontinuities, which often arise at stopping points. The deposition time for each layer was approximately 20 s, and the complete wall fabrication process took approximately 16m:40s.

Table 2 shows the process parameters used for the fabrication of the straight wall, while Table 3 shows its geometric parameters.

Table 2. WAAM-GMA process parameters used in wall fabrication.

Process parameter	Value
Voltage	19 V
Contact Tip to Work Distance	15 mm
Wire Feed speed	5.8 m/min
Gas flow rate	30 L/min
Travel speed	60 cm/min

Table 3. Programmed and final geometric parameters of the wall.

Parameter	Dimension
Span	200 mm
Number of layers	50
Layer’s height	~1.1 mm
Total wall height	~55 mm
Wall thickness	~6 mm

Fig. 1(a) shows the procedure adopted for capturing thermal cycles during layers deposition. The camera was positioned ~350 mm from the center of the base plate, a distance that allowed data capture without significant loss of thermal image quality, thus ensuring a good level of resolution.

Fig. 1(b) shows the schematic front view of the preform, with its main dimensions, on which five vertical lines (named A to E) were placed, used as a reference throughout the experiments. The points where the thermal cycles were captured were located over line C, in the center of the wall. Such line, in turn, was divided into 10 regions, each comprising five layers of deposited material.

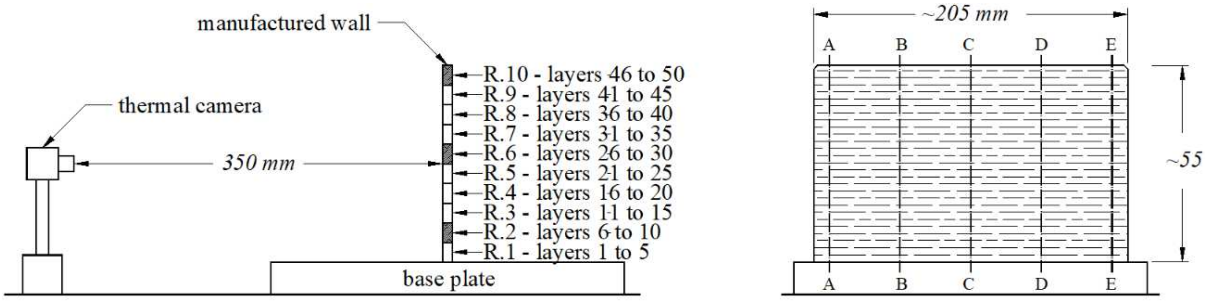


Fig. 1 Simplified image of the thermal cycle measurement system: a) camera position relative to the center of the baseplate and b) approximate final dimensions and reference columns (A to E)

Table 4 shows the list of layers for which thermal cycle graphs have been generated. To determine which graph corresponds to a specific layer, the peaks of the graphs were counted; each peak represents a specific layer, and the highest peak indicates the layer under analysis. Not all layers had graphics due to the camera resolution, which is related to the pixels.

Table 4. Layers for which thermal cycle graphs have been generated.

Region (layers)	**Layers that generated graphs**
Region 2 (6 a 10)	6 e 7
Region 3 (11 a 15)	12, 14 e 15
Region 4 (16 a 20)	17, 18, 19 e 20
Region 5 (21 a 25)	22 e 25
Region 6 (26 a 30)	27 e 29
Region 7 (31 a 35)	32, 34 e 35
Region 8 (36 a 40)	36 e 39
Region 9 (41 a 45)	41, 44 e 45
Region 10 (46 a 50)	47, 49 e 50

However, only the three shaded areas depicted in Fig. 1(a) were targeted for analysis, namely: *i)* region 2 (layers 6 to 10): near the base plate, *ii)* region 6 (layers 26 to 30): located at the midpoint of the wall's height, and *iii)* region 10 (layers 46 to 50): terminal region.

In summary, each temperature sampling point – regions 2, 6, and 10 over column C – experienced sequential temperature peaks with an approximate period of 20 s (corresponding to the deposition time of a layer).

Fig. 2 shows illustrative thermal images. The frames shown correspond to regions 2 and 10. At the top of the wall, the torch performing the deposition is visualized. The temperature values formed an Excel file, which was subsequently processed in the Octave program to generate graphs.

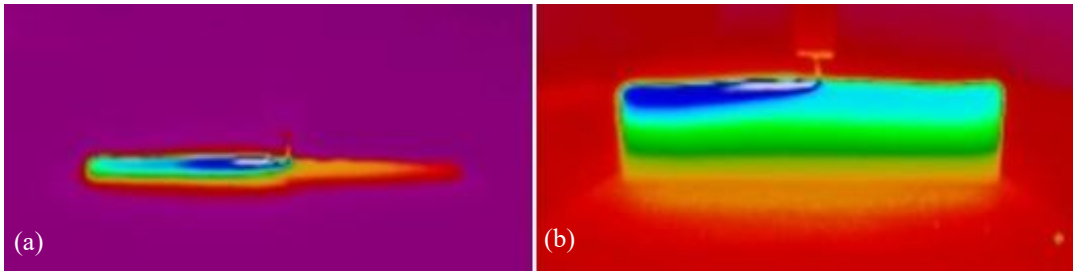


Fig. 2 Pictures in the center of the wall: a) region 2: layers 6 to 10 and b) region 10: layers 46 to 50

The treatment of temperature data included suppressing values prior to deposition. This is necessary because the camera records infrared radiation (and not visual images) that is subsequently converted into temperature values. Therefore, the temperature dataset related to a specific point must be broken down into two parts: *i)* prior to deposition (period in which the camera captures the temperature of the air, heated by the deposition of previous layers, or of the welding torch itself) and *ii)* from the moment of material deposition onwards.

Fig. 3 shows an example of a complete thermal cycle, as captured by the camera. This is the sixth layer deposited.

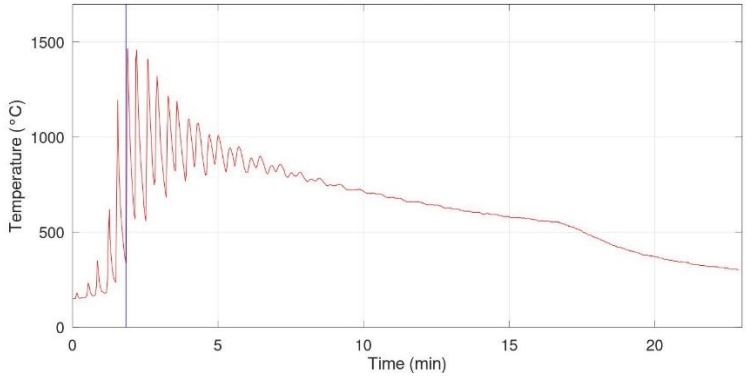


Fig. 3 Original graph of the 6th layer, in which a vertical line splits the peaks before and after deposition

The larger peak represents the moment when the torch passes over the point of analysis, depositing the material. A blue vertical line was inserted over this graph, separating the temperatures before (peaks on the left) and after deposition (peaks on the right).

Finally, the temperature data processing stage included, for each generated graph, shifting the origin of the time axis so that this origin corresponded to the instant of material deposition. This was necessary because temperature data collection began at the instant of electric arc initiation and extended throughout the preform fabrication process. Using the graph in Fig. 3 as an example, the origin indicates the arc ignition; however, the relevant data are located to the right of the blue vertical line, which should henceforth be regarded as the temporal reference.

Regarding the preparation of samples for microstructural analysis, step sanding was employed with sandpaper of 80 to 200 grit, followed by two-stage polishing with alumina of medium granulometry of 1 µm and 0.5 µm. The chemical agent was prepared based on the work of He et al. [29], being known as Beraha (15 ml of HCl + 85 ml of distilled water + 1 g of Potassium Metabisulfite) with an immersion time of 10 s.

The quantification of the austenite phase was performed using a quantitative metallographic analysis technique by image processing. The proportion of phases was based on the intensity of the gray color found in digitized images using image processing software, in this case ImageJ. In each section, 10 areas were measured in distinct locations for subsequent calculation of the average and standard deviation.

The Vickers hardness tests, in turn, were performed on the hatched regions in Fig. 1(a). The criteria of the ASTM E92-23 standard [30] were followed using a load of 100 kgf with an application time of 10 s. In addition, 5 measurements were taken in each section, for subsequent calculation of the average and standard deviation.

3 Results and relevant remarks

As previously mentioned, after the preform fabrication, the temperature data corresponding to regions 2, 6, and 10 of column C (Fig. 1) were selected and processed, and the respective thermal cycles were plotted. Subsequently, the following analyses were performed in the same regions: *i)* determination of austenite and ferrite proportions, and *ii)* Vickers hardness. Additionally, external dimensions of the wall, and its fluctuation, were

measured. The results obtained were compared with those reported by researchers who used similar materials and deposition techniques.

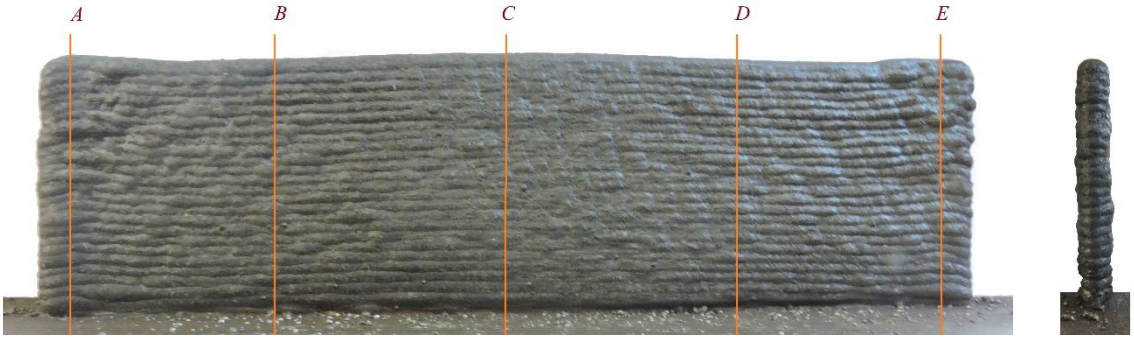
3.1 Average voltage and current values and geometric characteristics of the preform

The process monitoring system indicated the following average voltage and current values: 17.8 V and 119 A. According to Dos Santos et al. [31], this small difference between the value programmed in the voltage control loop (in this case, 19 V) and The measured effective value is due to natural fluctuations in the deposition process that are related to the physics of metal transfer from the wire, in addition to the possibility of a calibration problem at the source. In turn, the measured current value, even though relatively low, was within the range usually observed in WAAM-GMA processes [32].

With the monitored voltage and current values, it is possible to calculate the heat input to the process using Equation 3 [33], where η is the arc efficiency, V is the voltage, I is the current and V_s is the welding speed of the deposition process. The heat input in the process, for an efficiency of 80 %, is 169.456 J/mm.

$$E = \eta \frac{V \, x \, I}{V_s} \quad (3)$$

The geometric evaluation involved measuring the height, thickness, and length of the manufactured wall, which front and side views are shown in Fig. 4. The programmed 200 mm displacement produced a wall with a final length of approximately 205 mm.



(a) (b)

Fig. 4 Manufactured wall with geometry evaluation lines: a) front view and b) lateral view

It is clearly noticeable that there are different heights along the preform, with higher values at the ends and, especially, in the center. Regarding thickness, the irregular shape of the piece – characteristic of the WAAM process – generated considerable fluctuation in the measured values. Table 5 shows the height and thickness values measured in each section.

Table 5. Height and thickness dimensions of the preform, measured over the columns shown in Fig. 4.

Column	Height (mm)	Thickness (mm)
A	*56.7*	*9.4*
B	*55.4*	*6.5*
C	*57.9*	*6.3*
D	*55.8*	*6.4*
E	*56.5*	*8.8*

The works of Iqbal et al. [32], Tomar et al. [34] and Suresh & Veeman [35] highlighted the importance of welding parameters in the final quality of the part, both in terms of geometry and mechanical properties. Because they are directly associated with the heat input of the process, current and voltage have a direct impact on the geometry obtained. High voltage values increase the arc length and promote wettability, producing wider and flatter beads. In its turn, current is responsible for the heat supplied to the weld pool and, the greater this heat, the greater the fluidity and penetration capacity of the molten metal.

The larger thickness and height values at the ends of the wall are related to the torch's sequential deceleration and acceleration occurring near the programmed span's edges (reversal of movement). In these areas, the travel velocity changes while the feeding speed remains constant. As a result, more material is deposited at the ends of the wall. However, this deposition occurs on a still fluid substrate, leading to lateral spread instead of achieving even greater height.

Conversely, as the torch approaches the center of the wall, the substrate is advanced in its solidification process and, consequently, the deposited material does not spread laterally as it does at the ends. As a result, greater height values are achieved in the center region.

3.2 Analysis of the obtained thermal cycles

In the study by Hejripour et al. [25], the Cr_{eq}/Ni_{eq}ratio was calculated based on the ferrite transformation temperature using the Fe–Cr–Ni pseudo-binary diagram containing 70 wt.% Fe. For the chemical composition of ER2209, a value of approximately 2.9 was obtained, corresponding to a temperature of 1120 °C at the point where it intersects the solvus line of the diagram.

Fig. 5 shows the thermal cycles curves of layers 7, 27, and 47, respectively belonging to regions 2, 6, and 10. Two horizontal lines were superimposed on the diagrams, at 1120 °C (ferrite transformation temperature) and 400 °C (temperature below which no further relevant transformations occur in the material). As mentioned earlier, the time elapsed between the deposition of two successive layers (i.e., the time between the peaks of the graphs) is ~20 s.

The thermal regime associated with the material deposited in the 7th layer was strongly influenced by two factors, both intense but antagonistic: *i)* the heat imposed during the deposition of the material, as well as during the deposition of subsequent layers, and *ii)* the heat removal by the base plate, which was initially at room temperature and had considerable mass, giving it a high dissipation capacity. These factors caused large temperature fluctuations, i.e., after deposition, the material underwent an immediate temperature drop from ~1550 °C to ~650 °C in ~10 s, after which it underwent a new heating ramp to ~1300 °C, caused by the deposition of the next layer.

It was also observed that the material, after deposition, underwent heating above the ferritic transformation line in the four subsequent layers (8 to 11). Therefore, the material transitioned between the fully ferritic phase (whose transformation was not actually completed due to the short time the material remained above 1120 °C) and the coexistence of ferrite and austenite. Finally, still referring to the graph in Fig. 5(a), an inflection point of the curve is observed at t = ~14.5 min, the moment when the wall fabrication is completed. However, even after the interruption of the heat input, the thermal inertia and the low effectiveness of the dissipation mechanisms provided a smooth temperature decay, slightly greater than that which had already been occurring. In summary, the material remained above 400 °C for a period of approximately 17 min, and in the initial 5 min, the average temperature was above 800 °C.

Regarding the graph corresponding to layer 27 [Fig. (5)b], it is relevant to point out that this layer is located halfway up the wall and, in this zone, the thermal cycle occurs under the following conditions: *i)* the region is relatively far from the base plate, which, in turn, has undergone progressive heating throughout the deposition of the layers; consequently, heat dissipation is delayed, as the main mechanism for this is convective; and *ii)* due to this condition, the material below the deposition layer is still at a high temperature. Consequently, the graph of the intermediate zone, when compared to the region adjacent to the base plate, reveals a higher level of temperatures. After the deposition of the 27th layer, the 10 subsequent temperature peaks are above the ferritic transformation line, compared to 4 in the previous region. As for the valleys, in the region near the base plate, all are within the region of coexistence of ferrite and austenite. In the 27th layer, after the material was deposited, approximately 7 layers were required for the minimum temperature (i.e., the valleys of the fluctuating signal) to enter the Ferrite+Austenite region. Thus, the deposited material remained within the ferritic region for approximately 3 minutes, a considerably longer time than that observed in the material near the base plate. Finally, arc suppression occurred approximately 7.5 minutes after the material was deposited. Note that the temperature remained practically above 800 °C until the moment of arc suppression and, due to this temperature level, the material remained above 400 °C for approximately 12 minutes.

Finally, in the graph corresponding to layer 47 [Fig. (5)c], a scenario like that described in the previous case is observed, namely: the material below the depositing layer was at a relatively high temperature and the heat exchange mechanisms were not very effective. The difference lies in the fact that layer 47 is very close to the end of the process. The knee observed in the previous graphs, corresponding to the moment of arc suppression, is not visible here. The material remained in the complete ferritic phase zone for approximately 1.5 min, when the electric arc was then suppressed, causing a gradual decay of the temperature. The material reaches a temperature of 400 ºC approximately 5 min after being deposited.

The complete preform fabrication process took approximately 16 min and 40 s, which also corresponds to the last inflection point in the graphs of Fig. 5.

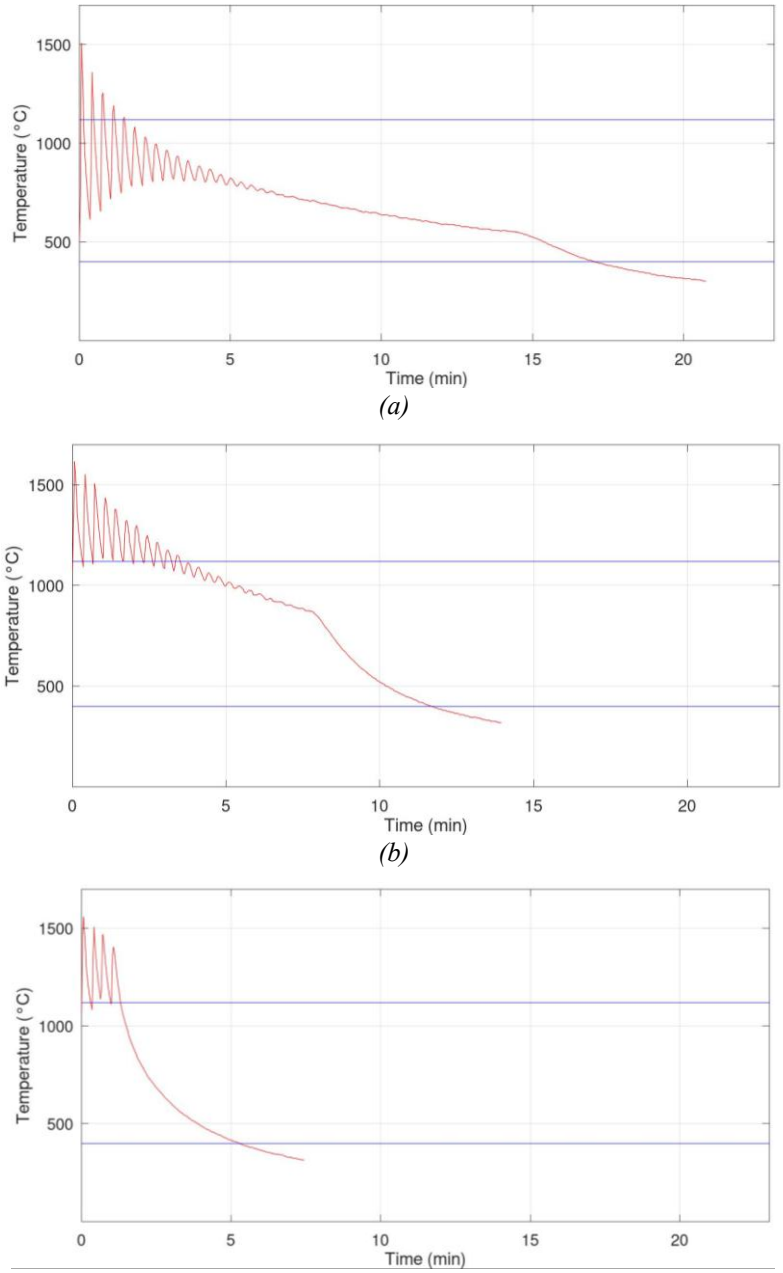
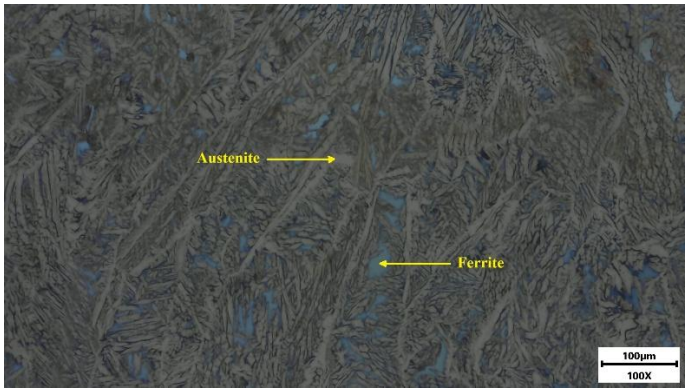


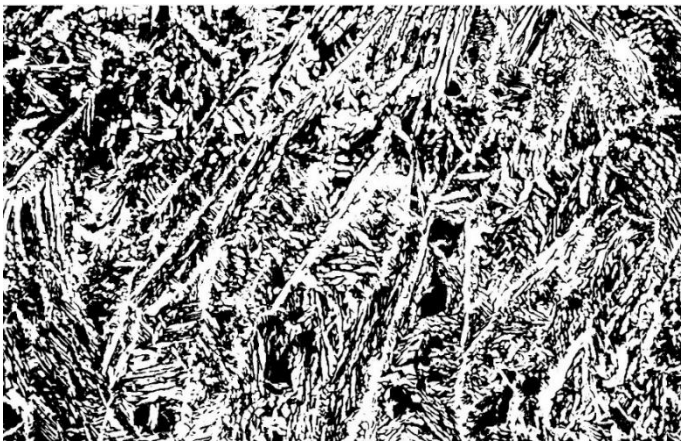
Fig. 5 Thermal cycles: a) 7th layer (region near the base plate), b) 27th layer (region at mid-height of the wall) and c) 47th layer (final deposition region)

3.3 Austenite content

A two-phase structure, shown in Fig. 6(a), was evidenced in microstructural samples. The dark or blue regions correspond to ferrite, while the slightly lighter regions represent austenite. Fig. 6(b) shows the image after digital processing, which made it binary. The material in Fig. 6 corresponds to layer 6 of region 2.



(a)



(b)

Fig. 6 Biphasic microstructure: a) revealed by chemical etching (Beraha) and b) after image processing

The austenite content by section is shown in Table 6. The equivalent bar diagram is presented in Fig. 7. Austenite contents above 70 % in the central region and close to 60 % in the terminal regions are highlighted.

Karunanithi et al. [26] found that the last layer of the wall they manufactured showed ferrite variation between 22 % and 27 %. In the present work, variation between 32.2 % and 38.6 % was observed, but it is relevant noticing that the data for region 10 includes a set of layers.

Table 6. Austenite content of the wall regions (region 1 was discarded due to dilution with base metal).

Region	Mean value	S.D.
2	59.59	3.29
3	66.24	3.26
4	69.76	1.87
5	69.25	1.43
6	71.50	1.97
7	69.73	2.56
8	71.27	2.34
9	69.76	2.05
10	64.65	3.24

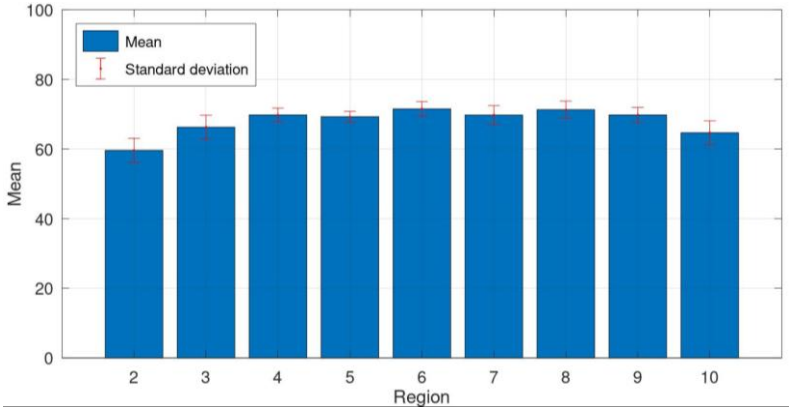


Fig. 7 Austenite quantification by regions in a bar graph

3.4 Hardness results

Table 7 shows the average Vickers hardness values measured, with their standard deviation, over the analysis regions. Fig. 8 shows the corresponding bar chart.

Table 7. Hardness mean and standard deviation values for the analyzed sections.

Region	Mean value	S.D.
2	376.2	5.70
6	385.3	9.39
10	386.1	14.95

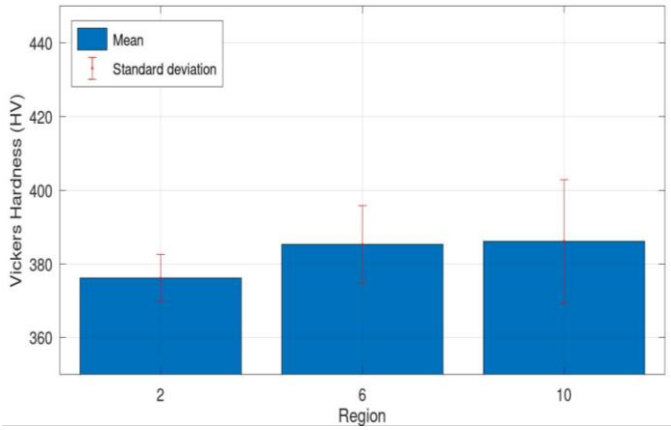


Fig. 8 Mean and standard deviation of Vickers hardness in bar graph

The hardness value in region 2 – lower compared to the other regions – was an unexpected result, since its ferrite content is higher. Conversely, regions with a higher austenite content (above 70 %) showed greater hardness.

According to Van et al. [36], Vickers hardness range between 240 HV and 320 HV in duplex stainless steel weld metals. Nevertheless, the hardness values presented here exceeded this range. The hypothesis proposed, which has not yet been verified, is that deleterious phases may have precipitated during the various temperature peaks.

3.5 Correlation of temperature cycles, austenite content and hardness

Fig. 10 shows the composition of the data relating to regions 2, 6 and 10. As already mentioned, the proximity of the lower layers to the base plate generated a higher cooling rate, which resulted in a higher ferrite content in the final composition. The first line of Fig. 10 [images (a), (b) and (c)] represents this region. The presence of ferrite grains, some of which are elongated, is noted, in a slightly greater quantity than in the other regions (shown in the second and third lines of Fig. 10).

The second line of Fig. 10 [images (d), (e) and (f)] represents region 6, in which very slow cooling resulted

in a higher austenite content in the final structure. As evidenced by the microstructural images (original and bichromatic), there is an extreme predominance of austenite in relation to ferrite.

Finally, region 10 is represented by the third line in Fig. 10 [images (g), (h) and (i)]. In this case, the temperatures remained above the solvus line (1120 °C) until the end of the process, when a relatively rapid cooling rate occurred, which restricted the transformation of the ferrite. The result is a microstructure intermediate, in terms of ferrite content, to the two previous regions.

The results point in the same direction as the arguments of Hejripour et al. [25] and Karunanithi et al. [26], according to which the marked disproportion between ferrite and austenite, in duplex steel preforms manufactured by the WAAM process, is a direct result of heat accumulation.

Fig. 9 presents the precipitate formation diagram specifically applied to duplex stainless steels. This diagram allows the temperatures obtained in the present study to be compared with the temperature and time ranges associated with the formation of deleterious phases in ER2205 steel, whose chemical composition is the closest to that of the ER2209 steel used in this study. The comparison between the two materials is presented in Table 8.

Table 8. Chemical comparison between ER2205 and ER2209 [26,37].

Material	Al	Cu	Cr	Mn	Mo	Ni	Si	C	N	P	S	Fe
ER2209	0,01	0,05	22,9	1,54	3,1	9	0,53	0,025	0,16	0,02	0,005	Bal.
ER2205	-	-	22,5	2	3,2	5,2	0,6	0,2	0,16	-	-	Bal.

According to Karunanithi et al. [23] and Zhang et al. [38], the precipitation of deleterious phases requires a period of exposure of the material to the temperature range in which the phenomenon occurs. For this reason, both studies adopted strategies to limit temperature, which contrasts with the uninterrupted layer deposition employed in present work.

In the case of 2205 steel, the diagram in Fig. 9 reveals a precipitate formation knee beginning after approximately 35 min of exposure to a temperature of ~850°C. Comparison of the diagrams of Figs. 10(a), 10(d), and 10(g) reveal that the intermediate region experienced the highest exposure to elevated temperatures. However, according to Fig. 9, this period would not be sufficient to cause the formation of deleterious phases. On the other hand, the hardness results shown in Table 8 did not show the expected direct relationship with the ferrite content. The high hardness values in the central and top regions of the wall indicate the possible formation of deleterious phases—potentially linked directly to the various thermal cycles the material underwent—which the diagram in Fig. 9 fails to explain. Therefore, the microstructure and mechanical properties of the weld metal generated by the deposition of ER2209 – usually used as filler metal in joints with ER2205 as the base metal – are likely to differ significantly from those of the base metal itself. Therefore, the hypothesis that ER2209 alloy electrodes, which represent a matching condition in conventional welded joints, do not achieve this equivalence in WAAM fabrication, should be tested in future studies.

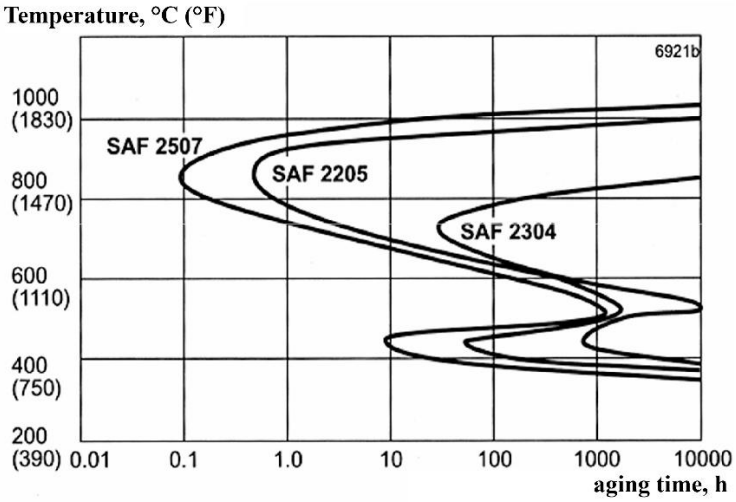


Fig. 9 Time-Temperature-Transformation Diagram for ER 2507, 2205 and 2304duplex stainless steels [39]

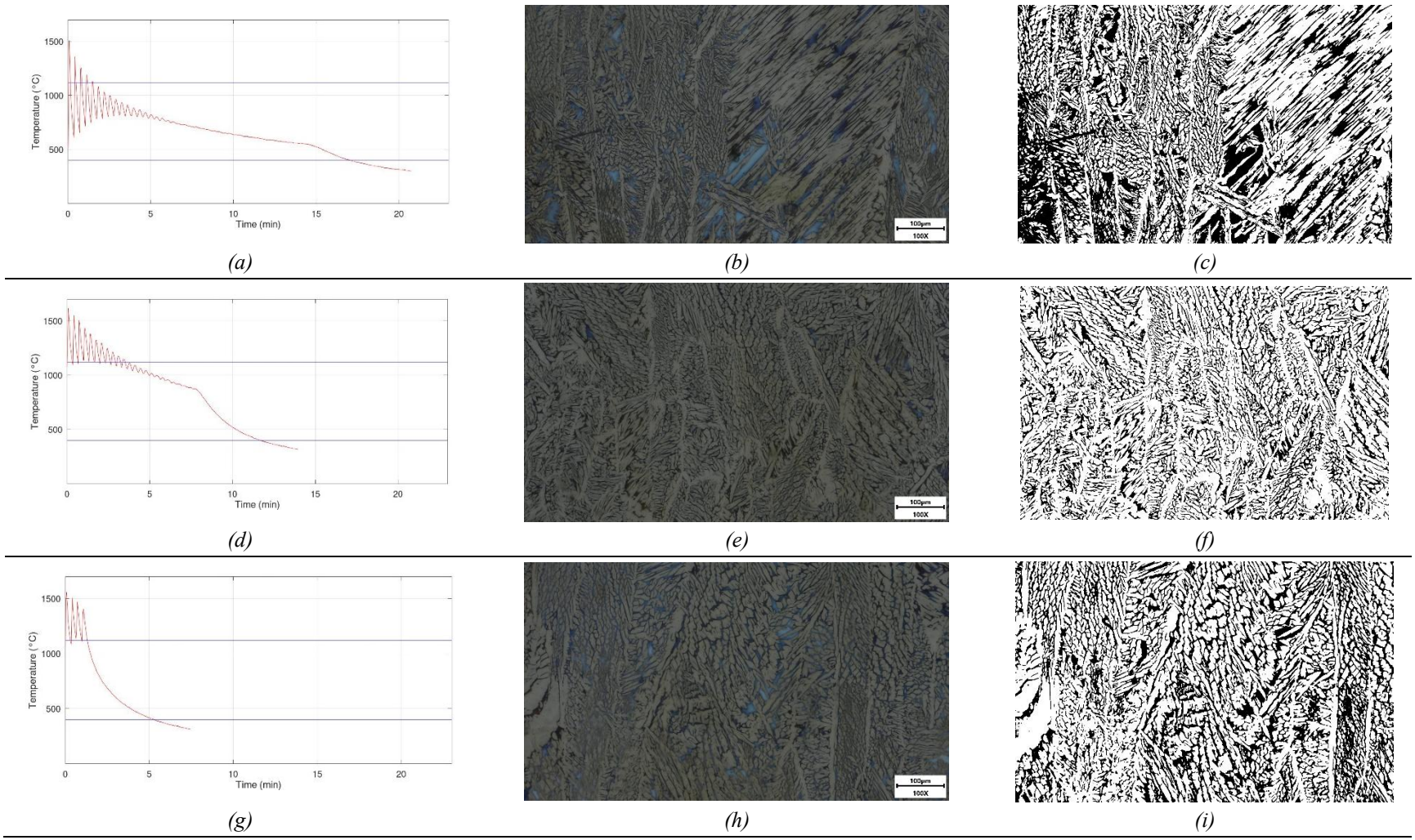


Fig. 10 Temperature diagrams, micrograph images and bichromatic images of Region 2: Line I [Images (a), (b), and (c)], Region 6: Line II [Images (d), (e), and (f)], and Region 10: Line III [Images (g), (h), and (i)]

4 Concluding remarks

This work presented an experimental study of the use of a computer vision system for thermal monitoring of the fabrication of a 50-layer linear preform, aiming to relate the phase changes found with the thermal cycles undergone. The following conclusions were obtained:

- The resulting geometry revealed that, during fabrication, the acceleration and deceleration of the torch caused fluctuations in the final dimensions of the part.
- The base plate showed a high capacity for heat removal in the initial deposition layers. However, throughout the process, this dissipation decreased due to heat accumulation.
- The material deposited in the first layers showed an austenite content close to 60%, a value not far from the 50% proportion considered ideal in duplex steels.
- From the 16th layer onwards, austenite content exceeded 70%, which is unacceptable for duplex steels.
- The austenite content decreased again in the region composed of the last five layers, where the temperature decayed more abruptly compared to the central region of the wall. However, even in this region, the ratio between ferrite and austenite remained far from the desired value.
-As a hypothesis the fluctuation in austenite content was attributed to the variations in the cooling rate, which was higher in the region near the base plate and in the final layers.
- The high austenite contents, above the limit of 70%, indicate the need to employ techniques to accelerate the cooling rate in the WAAM-GMA process or, when possible, post-processing to balance the phases.
- The thermal camera proved to be a very versatile, reliable, and inexpensive tool for monitoring the WAAM process.

Referencies

[1] H. FORD, Today and Tomorrow (Newly Annotated and Illustrated): Timeless Wisdom for a Modern Digital Age, 2018.

[2] J. LEE, B. BAGHERI, H.A. KAO, A Cyber-Physical Systems architecture for Industry 4.0-based manufacturing systems, Manuf. Lett. 3 (2015) 18–23. https://doi.org/10.1016/j.mfglet.2014.12.001.

[3] A. SURESH, R. UDENDHRAN, G. YAMINI, Internet of things and additive manufacturing: Toward intelligent production systems in industry 4.0, Internet of Things for Industry 4.0: Design, Challenges and Solutions (2020) 73–89.

[4] V.A. WANKHEDE, S. VINODH, Application of total interpretive structural modeling for analyzing factors of additive manufacturing and industry 4.0 integration, Rapid Prototyp. J. 27 (2021) 1591–1608. https://doi.org/10.1108/RPJ-02-2021-0028.

[5] M. KHORASANI, J. LOY, A.H. GHASEMI, E. SHARABIAN, M. LEARY, H. MIRAFZAL, P. COCHRANE, B. ROLFE, I. GIBSON, A review of Industry 4.0 and additive manufacturing synergy, Rapid Prototyp. J. 28 (2022) 1462–1475. https://doi.org/10.1108/RPJ-08-2021-0194.

[6] E.A. ALBERTI, L.J. DA SILVA, A.S.C.M. D'OLIVEIRA, Additive manufacturing: the role of welding in this window of opportunity, Welding International 30 (2016) 413–422. https://doi.org/10.1080/09507116.2015.1096513.

[7] D.D. CAMACHO, P. CLAYTON, W.J. O'BRIEN, C. SEEPERSAD, M. JUENGER, R. FERRON,

S. SALAMONE, Applications of additive manufacturing in the construction industry – A forward-looking review, Autom. Constr. 89 (2018) 110–119. https://doi.org/10.1016/j.autcon.2017.12.031.
[8] F. WENG, Y. CHEW, Z. ZHU, X. YAO, L. WANG, F.L. NG, S. LIU, G. BI, Excellent combination of strength and ductility of CoCrNi medium entropy alloy fabricated by laser aided additive manufacturing, Addit. Manuf. 34 (2020). https://doi.org/10.1016/j.addma.2020.101202.
[9] C. SHEN, Z. PAN, Y. MA, D. CUIURI, H. LI, Fabrication of iron-rich Fe-Al intermetallics using the wire-arc additive manufacturing process, Addit. Manuf. 7 (2015) 20–26. https://doi.org/10.1016/j.addma.2015.06.001.
[10] W. ZHAI, P. WANG, F.L. NG, W. ZHOU, S.M.L. NAI, J. WEI, Hybrid manufacturing of γ-TiAl and Ti–6Al–4V bimetal component with enhanced strength using electron beam melting, Compos. B Eng. 207 (2021). https://doi.org/10.1016/j.compositesb.2020.108587.
[11] W. ZHAI, Z. ZHU, W. ZHOU, S.M.L. NAI, J. WEI, Selective laser melting of dispersed TiC particles strengthened 316L stainless steel, Compos. B Eng. 199 (2020). https://doi.org/10.1016/j.compositesb.2020.108291.
[12] K. TREUTLER, V. WESLING, The current state of research of wire arc additive manufacturing (WAAM): a review, Applied Sciences (2021). https://www.mdpi.com/2076-3417/11/18/8619 (accessed November 28, 2024).
[13] D.F. GIAROLLO, C.C.P. MAZZAFERRO, J.A.E. MAZZAFERRO, Effect of filler material on sliding wear resistance of a structural steel welded by GMAW, Revista Materia 24 (2019). https://doi.org/10.1590/S1517-707620190003.0780.
[14] Q. HAN, J. GAO, C. HAN, G. ZHANG, Y. LI, Experimental investigation on improving the deposition rate of gas metal arc-based additive manufacturing by auxiliary wire feeding method, (n.d.). https://doi.org/10.1007/s40194-020-00994-0/Published.
[15] B. WU, Z. PAN, D. DING, D. CUIURI, H. LI, J. XU, J. NORRISH, A review of the wire arc additive manufacturing of metals: properties, defects and quality improvement, J. Manuf. Process. 35 (2018) 127–139. https://doi.org/10.1016/j.jmapro.2018.08.001.
[16] W. ZHAI, N. WU, W. ZHOU, Effect of Interpass Temperature on Wire Arc Additive Manufacturing Using High-Strength Metal-Cored Wire, Metals (Basel). 12 (2022). https://doi.org/10.3390/met12020212.
[17] R.N. GUNN, Duplex stainless steels: microstructure, properties and applications, 1997.
[18] G. ZILLI, F. FATTORINI, E. MAIORANA, Application of Duplex Stainless Steel for Welded Bridge Construction in Aggressive Environment, (2007).
[19] J. DAHLBERG, D. PETERSON, R. MEDLOCK, T. LOGAN, R.F. SOUGATA, Guide for Orthotropic Steel Deck Level 1 Design, Washington DC, 2022.
[20] R.J. CONNOR, J.W. FISHER, W. V. GATTI, S. ROY, F.E. BARTHELEMY, E.J. KAUFMANN, Manual for Design, Construction and Maintenance of Orthotropic Steel Deck Bridges, Washington DC, 2012.
[21] S. PATRA, A. AGRAWAI, A. MANDAL, A.S. PODDER, Characteristics and Manufacturability of Duplex Stainless Steel: A Review, Transactions of the Indian Institute of Metals 74 (2021) 1089–1098. https://doi.org/10.1007/s12666-021-02278-7.
[22] J.C. LIPPOLD, D.J. KOTECKI, Welding metallurgy and weldability of stainless steels, 2005.
[23] D.J. KOTECKI, T.A. SIEWERT, WRC-1992 Constitution Diagram for Stainless Steel Weld Metals: A Modification of the WRC-1988 Diagram, AWS Annual Meeting (1992) 171–178.
[24] S. ATAMERT, J.E. KING, Elemental partitioning and microstructural development in duplex stainless steel weld metal, Acta Metallurgica et Materialia 39 (1991) 273–285.
[25] F. HEJRIPOUR, F. BINESH, M. HEBEL, D.K. AIDUN, Thermal modeling and characterization of wire arc additive manufactured duplex stainless steel, J. Mater. Process. Technol. 272 (2019) 58–71. https://doi.org/10.1016/j.jmatprotec.2019.05.003.
[26] S.P. KARUNANITHI, R.K. ARASAPPAN, S.S. NALLATHAMBI, Microstructural Evolution, Mechanical and Electrochemical Performance of Duplex Stainless Steel Fabricated by Wire Arc

Additive Manufacturing with ER2209 Filler Wire, Steel Res. Int. (2024). https://doi.org/10.1002/srin.202400425.
[27] H. CHOI, J.M. ADAMCZYK, B.A. HERNANDEZ-SANCHEZ, E.K. KOSS, P.J. NOELL, S.R. SPIAK, R. V. PUCKET, K. ESCARCEGA-HERRERA, A.S. LOVE, E. KARASZ, V.S. NEARY, M.A. MELIA, M.J. HEIDEN, Wire arc additive manufactured A36 steel performance for marine renewable energy systems, International Journal of Advanced Manufacturing Technology 132 (2024) 4677–4688. https://doi.org/10.1007/s00170-024-13585-w.
[28] F.D. GUERMESA, H.G. LEMU, Y.W. ADUGNA, M.D. HARSIBO, Residual Stresses in Wire Arc Additive Manufacturing Products and Their Measurement Techniques: A Systematic Review, Applied Mechanics 5 (2024) 420–449. https://doi.org/10.3390/applmech5030025.
[29] Y. HE, Z. LIU, L. YANG, Y. ZHANG, W. LU, Microstructure, Mechanical Properties, and Corrosion Resistance of ER2209 Duplex Stainless Steel Manufactured by Plasma Arc Welding, Transactions of the Indian Institute of Metals 77 (2024) 2879–2886. https://doi.org/10.1007/s12666-024-03382-0.
[30] W.C.PA. ASTM International, Standard Test Methods for Vickers Hardness and Knoop Hardness of Metallic Materials., (2023).
[31] E.B.F. DOS SANTOS, L.H. KUROIWA, A.F.C. FERREIRA, R. PISTOR, A.P. GERLICH, On the visualization of gas metal arc welding plasma and the relationship between arc length and voltage, Applied Sciences (Switzerland) 7 (2017). https://doi.org/10.3390/app7050503.
[32] H. IQBAL, A. ASCARI, A. FORTUNATO, E. LIVERANI, Elucidating the effects of metal transfer modes and investigating the material properties in wire-arc additive manufacturing (WAAM), Progress in Additive Manufacturing 10 (2025) 3335–3360. https://doi.org/10.1007/s40964-024-00808-5.
[33] T. Kik, Predykcja własności złączy spawanych z wykorzystaniem zaawansowanych modeli źródeł ciepła, Wydawnictwo Politechniki Śląskiej, 2022.
[34] B. TOMAR, S. SHIVA, T. NATH, A review on wire arc additive manufacturing: Processing parameters, defects, quality improvement and recent advances, Mater. Today Commun. 31 (2022). https://doi.org/10.1016/j.mtcomm.2022.103739.
[35] S. GAIN, D. VEEMAN, A review on advances and challenges in wire arc additive manufacturing: Process parameters, microstructural evolution and material performance across alloys, J. Alloys Compd. 1029 (2025) 180735.
[36] N.L. VAN, MEELKER H., HILKES J., Welding duplex and super-duplex stainless steels, Welding in the World (1993).
[37] H. LIU, T. LI, R. LI, K. QI, L. QIAO, S. LIU, H. SUN, G. SONG, Evolution of joint microstructure and corrosion properties of 2205 duplex stainless steel by laser-TIG hybrid welding with high efficiency, Journal of Materials Research and Technology 39 (2025) 8132–8146. https://doi.org/10.1016/j.jmrt.2025.11.062.
[38] Y. ZHANG, F. CHENG, S. WU, The microstructure and mechanical properties of duplex stainless steel components fabricated via flux-cored wire arc-additive manufacturing, J. Manuf. Process. 69 (2021) 204–214. https://doi.org/10.1016/j.jmapro.2021.07.045.
[39] A.A. VICENTE, P.A. D'SILVA, R.L. DE SOUZA, I.L. DOS SANTOS, R.R. DE AGUIAR, A.B. BOTELHO JUNIOR, The use of duplex stainless steel filler metals to avoid hot cracking in GTAW welding of austenitic stainless steel AISI 316L, International Journal of Advanced Engineering Research and Science 7 (2020) 345–355. https://doi.org/10.22161/ijaers.76.43.